C. Y. Zhang
MIIT Key Laboratory of Multifunctional Lightweight Materials and Structures, College of Aerospace Engineering, Nanjing University of Aeronautics and Astronautics, Nanjing 210016, China
e-mail: zhangchunyu@nuaa.edu.cn

Y. Y. Liu
MIIT Key Laboratory of Multifunctional Lightweight Materials and Structures, College of Aerospace Engineering, Nanjing University of Aeronautics and Astronautics, Nanjing 210016, China
e-mail: liuyanyan@nuaa.edu.cn

T. I. Bhaiyat
School of Mechanical, Industrial and Aeronautical Engineering, University of the Witwatersrand, Johannesburg 2000, South Africa
e-mail: taahirbhaiyat01@gmail.com

S. W. Schekman
School of Mechanical, Industrial and Aeronautical Engineering, University of the Witwatersrand, Johannesburg 2000, South Africa
e-mail: sjouke.schekman@wits.ac.za

T. J. Lu
State Key Laboratory of Mechanics and Control of Mechanical Structures, Nanjing University of Aeronautics and Astronautics, Nanjing 210016, China;
MIIT Key Laboratory of Multifunctional Lightweight Materials and Structures, Nanjing University of Aeronautics and Astronautics, Nanjing 210016, China;
State Key Laboratory for Strength and Vibration of Mechanical Structures, Xi'an Jiaotong University, Xi'an 710049, China
e-mail: tjlu@nuaa.edu.cn

T. Kim[1]
MIIT Key Laboratory of Multifunctional Lightweight Materials and Structures, Nanjing University of Aeronautics and Astronautics, Nanjing 210016, China;
State Key Laboratory for Strength and Vibration of Mechanical Structures, Xi'an Jiaotong University, Xi'an 710049, China
e-mail: tongbeum.kim@nuaa.edu.cn

Impingement Cooling by Multiple Asymmetric Orifice Jets

This study presents impingement cooling from a flat plate by multiple asymmetric jets. Such jets are discharged through blunt-edge inline orifice holes with a thickness-to-diameter ratio of $t/D_j = 0.5$ and a jet-to-jet spacing of $T/D_j = 4.0$, at the Reynolds number of 20,000. First, fluidic features are established both in free exit and with impingement, at varying short target spacing (e.g., $H/D_j \leq 4.0$). Second, thermal characteristics of the jet impingement are elucidated. Results demonstrate that, due to a skewed incidence of the coolant stream upstream of concave orifice holes, the resulting multiple orifice jets are asymmetric and skewed relative to the orifice axis. These results mimic multiple fluidically inclined jets. However, asymmetric entrainment that takes place causes faster mixing with the surrounding fluid at rest as well as faster decay of momentum. This shows more effective cooling from a flat plate for the relatively short H/D_j range than conventional symmetric orifice and nozzle jets. [DOI: 10.1115/1.4053330]

Keywords: asymmetric jet, orifice jet, concave blunt orifice, jet impingement, multiple jets

[1]Corresponding author.
Contributed by the Heat Transfer Division of ASME for publication in the JOURNAL OF HEAT TRANSFER. Manuscript received June 12, 2021; final manuscript received December 13, 2021; published online January 18, 2022. Assoc. Editor: Poh Seng Lee.

1 Introduction

The study of jet-flow structures is largely driven by impingement cooling techniques, with which large heat fluxes can be dissipated. Jet impingement has been used effectively in the thermal management of gas turbine blades, furnaces, extruded materials, electronics, and photovoltaic cells. This is attributed to the characteristically higher heat transfer rate that can be achieved with impingement cooling, relative to other conventional single-phase heat transfer methods. In consideration of gas turbine blades, specifically, the jet is formed when the coolant stream passes through a hole in the perforated internal structure. The relative thickness of such a hole typically falls within the range of $0.5 < t/D_j < 5.0$: structural integrity, dimension constraints, and manufacturability of the perforated structure are the primary design criteria that dictate the hole size. At the lower end of this spectrum, $t/D_j = 0.5$, the jet is expected to behave as an orifice jet.

Previously, orifice jets have been studied, with a relative thickness in the range of $0.09 < t/D_j < 0.5$ considered [1–5]. Common to each of the foregoing studies is a separated flow that develops at the orifice inlet and cannot reattach before exiting the perforated structure. This causes large vortical flow structures and a characteristic vena contracta. In existing single and multiple orifice jet studies [6–15], the jets are generated through a flat orifice plate by streams approaching the perforated holes parallel to their axis. On the other hand, in a gas turbine blade, the coolant is fed from the root of the blade and subsequently moves through serpentine channels or a feed passage (as shown in Fig. 1). From there, the coolant flows through the perforated structure as jets, and possibly orifice jet flows. Due to coolant streams turning upstream of the perforated holes associated with the above-mentioned geometric and fluidic configurations, the jets are not expected to be axisymmetric. Further still, the perforated structure will not necessarily be flat as shown in Fig. 1, which may further instigate nonaxisymmetric jet flows. To the best of the authors' knowledge, how orifice jet asymmetry affects impingement heat transfer remains elusive.

To better understand impingement heat transfer characteristics in such an engineering relevant configuration, this study aimed to address the following questions.

(1) How did single and multiple orifice jets discharged through a concave orifice with the biased incidence of coolant supply become fluidically asymmetric?
(2) How did impingement heat transfer on a flat plate differ between conventional symmetric orifice jets and asymmetric orifice jets, especially within short jet exit-to-flat plate spacing?
(3) How did the impingement heat transfer of multiple asymmetric orifice jets differ from that of single asymmetric orifice jet?

To this end, the thermofluidic aspects of five equally spaced orifice jets were experimentally investigated. The jets had the fixed jet-to-jet spacing of $T/D_j = 4.0$ and were discharged through a scaled-up concave orifice plate having a thickness of $t/D_j = 0.5$. Each jet was produced at a sufficiently high jet Reynolds number ($\mathrm{Re}_j = 20{,}000$), thus ensuring a fully turbulent jet. A series of experiments were carried out for relatively short impingement spacing (i.e., $H/D_j \leq 4.0$), including flow visualization, axial time-averaged velocity measurements, and local heat transfer mapping on an isoflux flat target surface cooled by both single and multiple orifice jets with a blunt edge.

2 Experimental Details

The test rig mainly consisted of two sections: for generating the jet and for its impingement. For the former section, to measure the mass flowrate of the jet, ambient air drawn by a centrifugal fan controlled via a frequency inverter was passed through a precalibrated turbine flowmeter. Downstream of this section, a cubic settling chamber, 0.5 m (width) × 0.5 m (height) × 0.5 m (depth), was connected, with a flow distributor plate placed at its mid-depth. A 1.0 m-long cylindrical chamber was connected to the settling chamber, via a flexible rubber pipe. Five inline holes with $D_j = 21$ mm in diameter and center-to-center spacing of $T/D_j = 4.0$, which loosely mimicked the value qualitatively extracted from a patent application [16], were drilled into the chamber as shown in Fig. 2(*a*). The thickness-to-orifice hole diameter ratio was thence $t/D_j = 0.5$.

Throughout the study, the jet Reynolds number was fixed at $\mathrm{Re}_j = 20{,}000$, defined based on the jet diameter (D_j), as

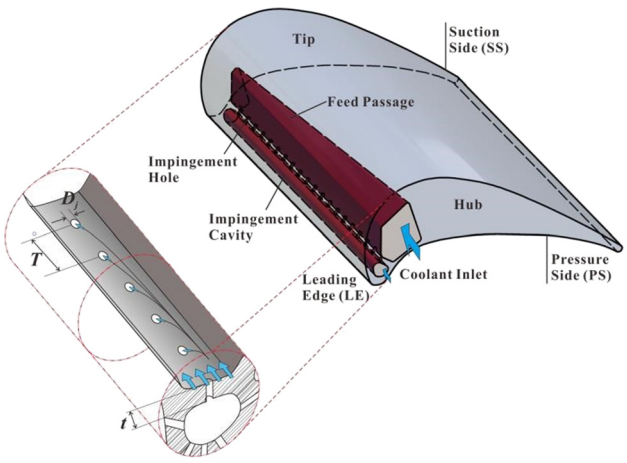

Fig. 1 Internal cooling at the leading edge of a gas turbine blade [16] with a simplified design employing multiple jets

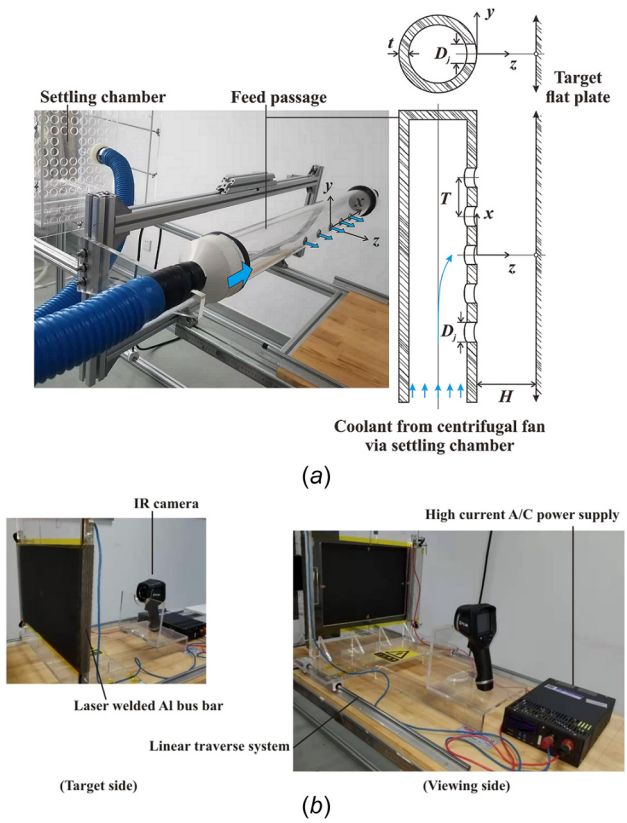

Fig. 2 Test setup: (*a*) photograph and (*b*) thermal mapping by an infrared camera

Table 1 Parameters of test conditions and test setup

Test parameter	Value
Density of air, ρ	1.19197 kg/m^3
Dynamic viscosity of air, μ	1.8277×10^{-5} Pa·s
Orifice diameter, D_j	0.021 m
Relative thickness, t/D_j	0.5
Orifice center-to-center spacing, T/D_j	4.0
Jet exit-to-flat target plate spacing, H/D_j	0.2, 0.5, 4.0
Jet Reynolds number, Re_j	20,000

$$\mathrm{Re}_j = \frac{\rho w_m D_j}{\mu} \tag{1}$$

where ρ and μ are the density and dynamic viscosity of air, respectively, and w_m is the mean jet velocity. Fluid properties obtained at local temperature and barometric pressure were detailed in Table 1.

To characterize the length of the potential core and the dissipation characteristics of each jet in free exit, a Pitot tube (KIMO, L-type, 3.0 mm in diameter) was connected to a digital micromanometer (TSI, 9565). This was incrementally traversed in the axial (z/D_j) and radial (r/D_j) coordinates via a two-axis linear traverse system. Centerline velocity measurements were conducted in increments of 5.0 mm, within the range of $0.0 < z/D_j < 20.0$. Radial profile of the axial velocity component of each jet was measured at $z/D_j = 0.0$, 1.0, 2.0, 3.0, and 4.0.

Following the method reported by Coleman and Steele [17], uncertainty associated with the axial velocity component measured along the centerline (or the z-axis) by the Pitot tube at $\mathrm{Re}_j = 20{,}000$ was estimated as

$$\frac{\delta w}{w} = \pm\sqrt{\left[\left(\frac{\delta p_t}{p_t - p_s}\right)^2 + \left(\frac{\delta p_s}{p_t - p_s}\right)^2\right] \times \left(\frac{1}{2}\right)^2} = \pm 0.37\% \tag{2}$$

where p_t is the stagnation pressure, and p_s is the static pressure. Thus, uncertainty of the jet Reynolds number was estimated as

$$\frac{\delta \mathrm{Re}}{\mathrm{Re}} = \pm\sqrt{\left(\frac{\delta D_j}{D_j}\right)^2 + \left(\frac{\delta w}{w}\right)^2} = \pm 0.379\% \tag{3}$$

where

$$\frac{\delta D_j}{D_j} = \pm\frac{0.02}{21} = \pm 0.095\% \tag{4}$$

To visualize the jet-flow patterns, the technique of ink-dye injection in a water-tunnel was used. The cylindrical chamber was submerged in an acrylic water container with 0.6 m (width) × 0.6 m (depth) × 0.6 m (height) in dimensions and located at the mid-depth of the container, and an orifice with $t/D_j = 0.5$ was drilled to the chamber. Two injection needles were installed at both sides of the orifice hole's exit, in the x–z plane, to trace (a) vortices shed from the periphery of the jet and (b) thickness of separated flows from the entrance of the orifice hole. To record the visualized flow patterns, a video camera (SONY FDR-AX45) was placed normal to the x–z plane. While the camera was operating at a high-speed mode, an auxiliary illumination system employing a multirow light emitting diode (LED) light bar was implemented from the bottom wall of the cubic water-tunnel.

For the impingement section, a flat plate with two different heat transfer setups, mounted vertically on a linear traverse system, was used to adjust the jet exit-to-target surface distance (H) along the jet axis. The first heat transfer setup in Fig. 2(*b*), mapped detailed local heat transfer distributions on the isoflux flat plate, 0.6 m wide and 0.3 m long, constructed using a 51 μm thick stainless-steel shim stock heater. Both ends of the heater were laser welded to 0.3 m long aluminum (Al) bus bars, to minimize voltage/current drop across the bus bars. Each bus bar was then fixed vertically to the edge of a 10 mm thick acrylic base plate (0.6 m wide and 0.6 m long), which acted to reduce possible vibrations of the heater due to jet impingement. An electric current typically of 54 A and 3.5 V (yielding an input heat of 189 W and a corresponding input heat flux of 1050 W/m^2) from an AC power supply was imposed across the heater through the bus bars. A central part of the acrylic base plate (0.38 m wide and 0.27 m long) was removed to generate an infrared (IR) viewing window, as shown in Fig. 2(*b*). However, this configuration yielded substantial heat losses, by radiation from both the impinging and back sides of the heater and natural convection from its back side as well as from the bus bars. As a result, the net heat removed effectively by jet impingement needed to be estimated and corrected. To this end, another heat transfer setup was constructed, employing an etched foil heater mounted on a flat plate that was fabricated from a bakelite material ($k \approx 0.18$ W/m K). The circular foil heater was 0.3 m in diameter and 0.3 mm in thickness. A film T-type thermocouple, 20 μm thick, was attached via a spray glue to the center of the foil heater. Another film T-type thermocouple, also 20 μm thick, was attached to the back side of a 10 mm thick base bakelite plate. With this thermocouple setup, conductive heat loss through the target plate could be estimated. Total heat losses via conduction and radiation were estimated, as detailed below.

Impingement heat transfer was evaluated using the Nusselt number (Nu), defined as

$$\mathrm{Nu} = \frac{h_s}{k_f/D_j} \tag{5}$$

where D_j is the orifice diameter, k_f is the thermal conductivity of air, and h_s is the convective heat transfer coefficient on the target plate

$$h_s = \frac{q''_{\mathrm{net}}}{T_s - T_e} \tag{6}$$

Here, q''_{net} is the net heat flux, and T_s and T_e are the local surface temperature (by film thermocouple) and the jet temperature (by bead thermocouple) at nozzle exit ($z/D_j = 0.0$), respectively. The net heat flux q''_{net} was obtained via energy balance, as

$$q''_{\mathrm{net}} = q''_t - q''_{\mathrm{cond}} - q''_{\mathrm{rad}} \tag{7}$$

where q''_t is the input heat flux supplied to the etched foil heater, and q''_{cond} and q''_{rad} are separately conduction and radiation heat losses. Conduction heat loss through the backside of target surface was estimated to be 5.0%, using Fourier's law. Radiation loss was calculated using the Stefan–Boltzmann law, as

$$q''_{\mathrm{rad}} = \epsilon\sigma(T_s^4 - T_a^4) \tag{8}$$

where ϵ is the emissivity, σ is the Stefan–Boltzmann constant, and T_a is the ambient temperature. The emissivity was taken to be 0.94 as estimated using an infrared camera (FLIR$^{\mathrm{TM}}$ T-Series), by inversely matching temperature reading from IR camera to that from the film thermocouple on the same location of target plate. It should be noted that, for commercial copper scoured to a shine, the emissivity is typically 0.07 at 20 °C. Resolution of temperature readings from the temperature scanner was 0.1 K for each thermocouple.

Based on heat transfer coefficient (h_s) calculated using Eq. (6), which is known at a particular location on the target plate especially at its stagnation point, the net heat flux emitted by the stainless-steel shim stock heater ($q''_{\mathrm{net,IR}}$) might be expressed as

$$q''_{\text{net, IR}} = h_s(T_{s,\text{IR}} - T_e) \tag{9}$$

Relative heat losses from the heater were estimated as

$$R_{\text{loss}} = 1 - \frac{q''_{\text{net, IR}}}{q''_{t,\text{IR}}} \tag{10}$$

The values of R_{loss} varied substantially, from 10% to 30% of total heat input to the heater, with specific values depending upon individual setups.

Uncertainty of the Nusselt number (Nu) is associated with the wall temperature T_s, the jet temperature at exit T_e, and various heat losses during the experiment. Uncertainty of radiant heat loss was calculated as

$$\frac{\delta q''_{\text{rad}}}{q''_{\text{rad}}} = \pm\sqrt{\left(\frac{\delta T_s \cdot T_s^3}{T_s^4 - T_e^4}\right)^2 \times 4^2 + \left(\frac{\delta T_e \cdot T_e^3}{T_s^4 - T_e^4}\right)^2 \times 4^2} = \pm 0.86\% \tag{11}$$

Concerning the bakelite flat surface, uncertainty of conduction heat loss through the flat plate was calculated as

$$\frac{\delta q''_{\text{cond}}}{q''_{\text{cond}}} = \pm\sqrt{\left(\frac{\delta T_s}{T_s - T_b}\right)^2 + \left(\frac{\delta T_s}{T_s - T_b}\right)^2} = \pm 0.73\% \tag{12}$$

Uncertainty of input heat flux was calculated based on the foil heater input voltage of $U = 153$ V and the input current of $I = 1.1$ A, as

$$\frac{\delta q''_t}{q''_t} = \pm\sqrt{\left(\frac{\delta U}{U}\right)^2 + \left(\frac{\delta I}{I}\right)^2} = \pm\sqrt{\left(\frac{1}{153}\right)^2 + \left(\frac{0.1}{1.1}\right)^2} = \pm 9.11\% \tag{13}$$

Hence, uncertainty of net heat flux was estimated as

$$\frac{\delta q''_{\text{net}}}{q''_{\text{net}}} = \pm\sqrt{\left(\frac{\delta q''_t}{q''_t - q''_{\text{cond}} - q''_{\text{rad}}}\right)^2 + \left(\frac{\delta q''_{\text{cond}}}{q''_t - q''_{\text{cond}} - q''_{\text{rad}}}\right)^2 + \left(\frac{\delta q''_{\text{rad}}}{q''_t - q''_{\text{cond}} - q''_{\text{rad}}}\right)^2} = \pm 9.26\% \tag{14}$$

Further, uncertainty associated with convective heat transfer coefficient was estimated as

$$\frac{\delta h_s}{h_s} = \pm\sqrt{\left(\frac{\delta q''_{\text{net}}}{q''_{\text{net}}}\right)^2 + \left(\frac{\delta T_s}{T_s - T_e}\right)^2 + \left(\frac{\delta T_e}{T_s - T_e}\right)^2} = \pm 9.28\% \tag{15}$$

Finally, uncertainty associated with the Nusselt number was estimated as

$$\frac{\delta \text{Nu}}{\text{Nu}} = \pm\sqrt{\left(\frac{\delta h_s}{h_s}\right)^2 + \left(\frac{\delta D_j}{D_j}\right)^2} = \pm 9.28\% \tag{16}$$

3 Results of a Single Asymmetric Orifice Jet

3.1 Free Jet Patterns. Prior to jet impingement cooling from a flat plate, an orifice jet was quantified in free exit. This jet was issued from a perforation located on the side of a cylindrical chamber, simulating a feed passage in Fig. 2(*a*). The cylindrical chamber was blocked at one end, forcing the coolant to flow from the open end through the chamber and out of the perforation on the side. Two factors that need to be considered with this setup are: (a) the perforation is located on a concave surface, and (b) the coolant is forced to undergo a change in direction before exiting. Both are expected to result in features unique to those reported in existing jet impingement studies.

Figure 3(*a*) displayed coolant flow through the orifice hole in the x–z plane. The core of the jet was skewed toward the positive x-axis and assumed the z'-direction, off from the orifice hole axis (z) by an angle (or skewness) of α. Coherent structure-like vortices were shed from the edge of the orifice hole, implying that shear layers formed at the periphery of the jet's core. The thickness of the shear layer on either side of the core differed, being thinner on the side to which the jet was skewed along the positive x direction. This was attributed to the differing angles of incidence between

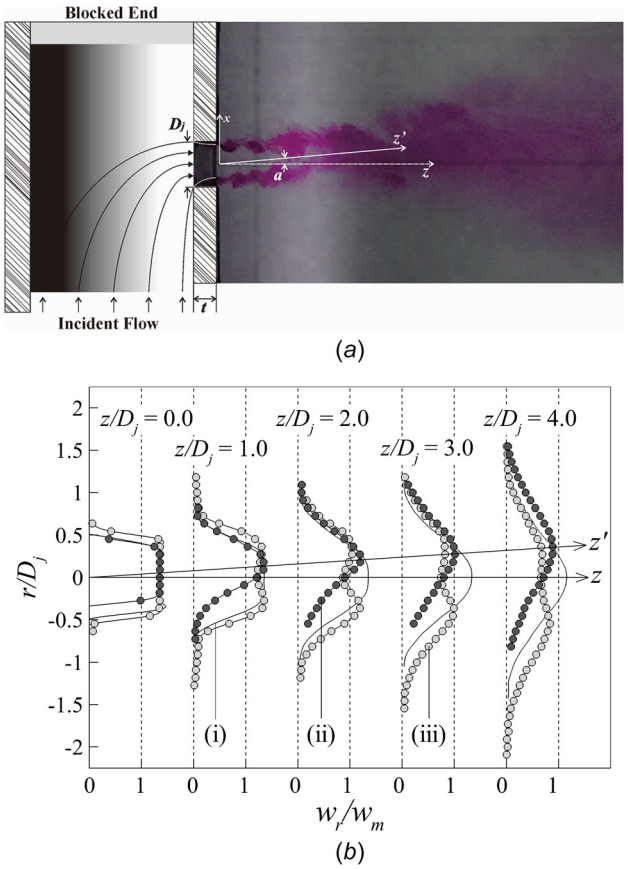

Fig. 3 Single asymmetric orifice jet ($t/D_j = 0.5$): (*a*) visualized flow pattern, and (*b*) velocity profiles, (i) for unbiased incident coolant stream, (ii) for a concave blunt orifice in x–z plane, and (iii) for a concave blunt orifice in y–z plane

the coolant stream and the edges of the orifice hole, which in turn caused dissimilar boundary layer formation on either side of the orifice hole.

From flow visualization, the exact extent of skewness measured from the z-axis could not be reliably quantified. Rather, it was estimated from velocity profiles measured in the x–z plane and plotted in Fig. 3(*b*). The velocity profiles in the y–z plane were also presented along with data from a flat orifice plate as reference; the latter, denoted as (i) in Fig. 3(*b*), was simply referred to as the reference jet hereon. The reference jet resulted in an axisymmetric velocity profile with respect to the z-axis. At the jet exit, the velocity profile of the reference jet was uniform, exhibiting a steep velocity gradient near its periphery. Consequently, the downstream axial momentum diffused radially due to entrainment in the shear layer. The velocity profile eventually became parabolic, with the peak velocity typically coinciding with the nominal jet axis (z).

In contrast, the orifice jet discharged from the concave orifice was distinctively nonaxisymmetric. Denoted as (ii) in Fig. 3(*b*), the peak of the parabolic velocity profile did not coincide with the z-axis but became skewed as noted in Fig. 3(*a*). With peak velocity in the x–y plane considered, the skewness toward the positive x-axis was found to be $\alpha \sim 5$ deg, following the z'-axis further downstream. In addition, for a given axial traverse plane, the magnitude of the peak axial velocity diminished faster than that of the reference jet.

In the y–z plane (denoted as (iii) in Fig. 3(*b*)), the nonaxisymmetric orifice jet was symmetric with respect to the z-axis. Given that the flow upstream of the orifice in the cylindrical chamber was symmetric in the y–z plane, the symmetry of the orifice jet in this plane should be expected. At exit, the orifice jet had a very similar profile to the reference jet in the y–z plane. However, downstream, this radial profile became a saddle-like profile, achieving a local minimum at the nominal jet axis (z) and a local maxima at about $r/D_j = \pm 0.5$ along the length of the jet. The radial extent of the diffused jet in this plane was almost the same as the reference jet. The magnitude of the peak velocity, however, was substantially reduced (to ~60% of the reference peak velocity) at $z/D_j = 4.0$.

In summary, the orifice jet formed via a concave blunt orifice tended to be highly diffused radially, especially in the y–z plane, causing substantially reduced axial momentum. Further, the jet axis in the x–z plane was skewed. Upon impingement on a flat target surface, these phenomena are expected to significantly affect local surface heat transfer.

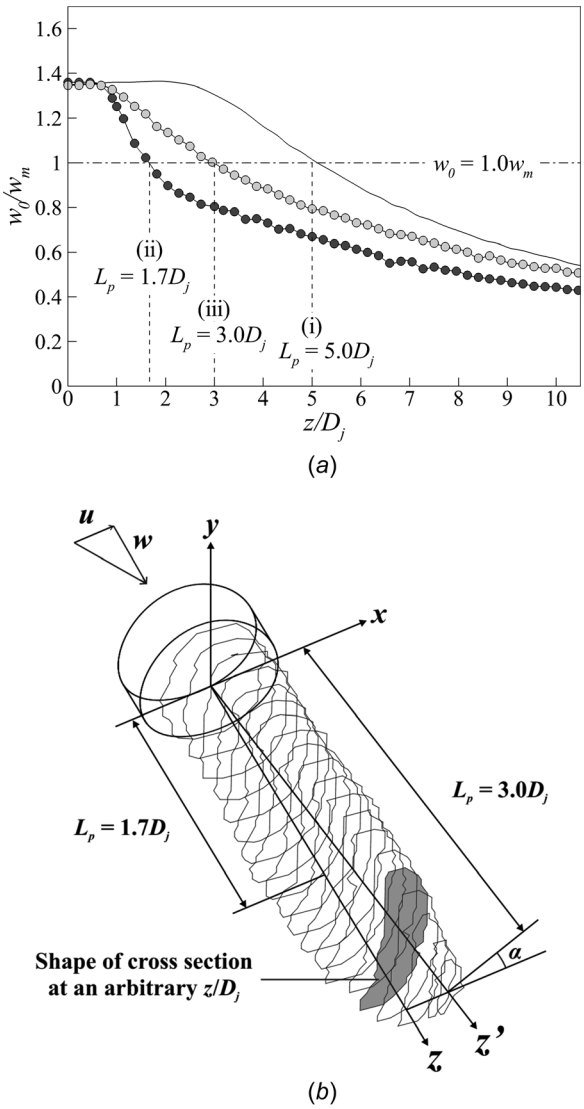

Fig. 4 Variation of potential core: (*a*) centerline velocity where (i) for a flat blunt orifice with $t/D_j = 0.5$, (ii) for a concave blunt orifice along z-axis, and (iii) for a concave blunt orifice along z'-axis, and (*b*) cross sections of potential core

3.2 Potential Core of a Free Jet. For a given jet, the length of its potential core plays an important role in determining local heat transfer distribution on an impinged target surface. Therefore, the variation of the jet's axial velocity along its axis needs to be quantified. Broadly speaking, two different methods had been used to define the potential core length, as outlined below.

In one method, commonly encountered in existing literature, the local centerline velocity is normalized against that at the jet exit (w_e). The position at which the normalized velocity decreases below 0.95 (or 0.98) marks the length of the potential core [18], beyond which the velocity decays rapidly. In another method, as summarized by Gauntner et al. [19], the potential core length is estimated by normalizing the local centerline velocity by the average jet velocity (w_m). In this definition, a log–log plot of the measured centerline velocity ratio w_0/w_m against z/D_j yielded a line with a slope of -1. The extension of the line to intersect the line of $w_0/w_m = 1.0$ then gave the length of the potential core.

In this study, with the second method adopted [19], the reference jet (denoted as (i) in Fig. 4) had a potential core length of $L_p = 5.0D_j$, which fell within the range reported by Gauntner et al. [19], i.e., $4.7D_j \leq L_p \leq 7.7D_j$. The concave orifice with an off-axis inlet flow, i.e., a nonaxisymmetric orifice jet—denoted as (ii) in Fig. 4, was approximately $1.7D_j$. This was substantially shorter than the typical range of potential core lengths reported [19]. With the skewed orifice jet accounted for, by measuring the centerline velocity along the z'-axis (denoted as (iii) in Fig. 4), the potential core length was found to be longer at $L_p = 3.0D_j$. Thus, it can be concluded that the potential core length for a nonaxisymmetric orifice jet is substantially shorter than that of both a symmetric orifice jet and a turbulent circular jet.

Figure 4(*a*) also demonstrates the importance of the distinction in how potential core length is determined. If the common method of normalizing against jet exit velocity was adopted, the potential core of an orifice jet would be the same regardless of whether velocity measurements were made along the z- or z'-axis, which was, however, obviously misleading. It was suspected that this similarity occurred due to a variation in the shape of the orifice jet potential core. To confirm this, the shape of the potential core was quantified using a series of isocurves that characterized the peripheries of the potential core at different z/D_j positions, as shown in Fig. 4(*b*). A series of planes parallel to the x–y plane (i.e., at different z/D_j) were selected, and the axial velocities in each selected z/D_j position were measured using the Pitot tube from the jet exit, in increments of $z/D_j = 1.0$. At each increment, upon comparing

the velocities with w_m, an isocurve denoting the cross-sectional boundary of the potential core was obtained using the criterion of $w_0/w_m < 1.0$. All the isocurves were mapped to show the peripheries of the potential core.

At any z/D_j, the potential core exhibited a unique crescent cross-sectional shape, previously not noted for orifice jet flows. This shape explains the saddle shaped radial velocity profiles in the y–z plane shown in Fig. 3(*b*). Further, when the jet impinges on a target surface, this shape is expected to result in a unique heat transfer distribution thereon.

3.3 Local Heat Transfer Distribution on an Isoflux Flat Plate. Overall temperature maps on an isoflux flat plate obtained with an IR thermal camera were plotted in Fig. 5(*a*), for three selected H/D_j values. For a given H/D_j value, the lower temperature (or higher heat transfer) regions coinciding approximately with the jet axis were nonaxisymmetric. In contrast, with fully developed round tube jets and typical orifice round jets, axisymmetric contours are usually encountered. Nonetheless, certain symmetry in the contours still exists, particularly with respect to the x-axis in the y–z plane.

The crescent shaped potential core in Fig. 4(*b*), caused the central regions to also exhibit a crescent shape, associated with higher convective heat transfer. This held for all H/D_j values considered. To elaborate this further, the temperature plots of Fig. 5(*a*) were used to calculate local Nusselt number distributions via Eq. (5). Figures 5(*b*)–5(*d*) plotted separately the radial distributions of the Nusselt number, in both the x–z and y–z planes, for $H/D_j = 0.5$, 2.0, and 4.0. Data points near the stagnation region obtained with

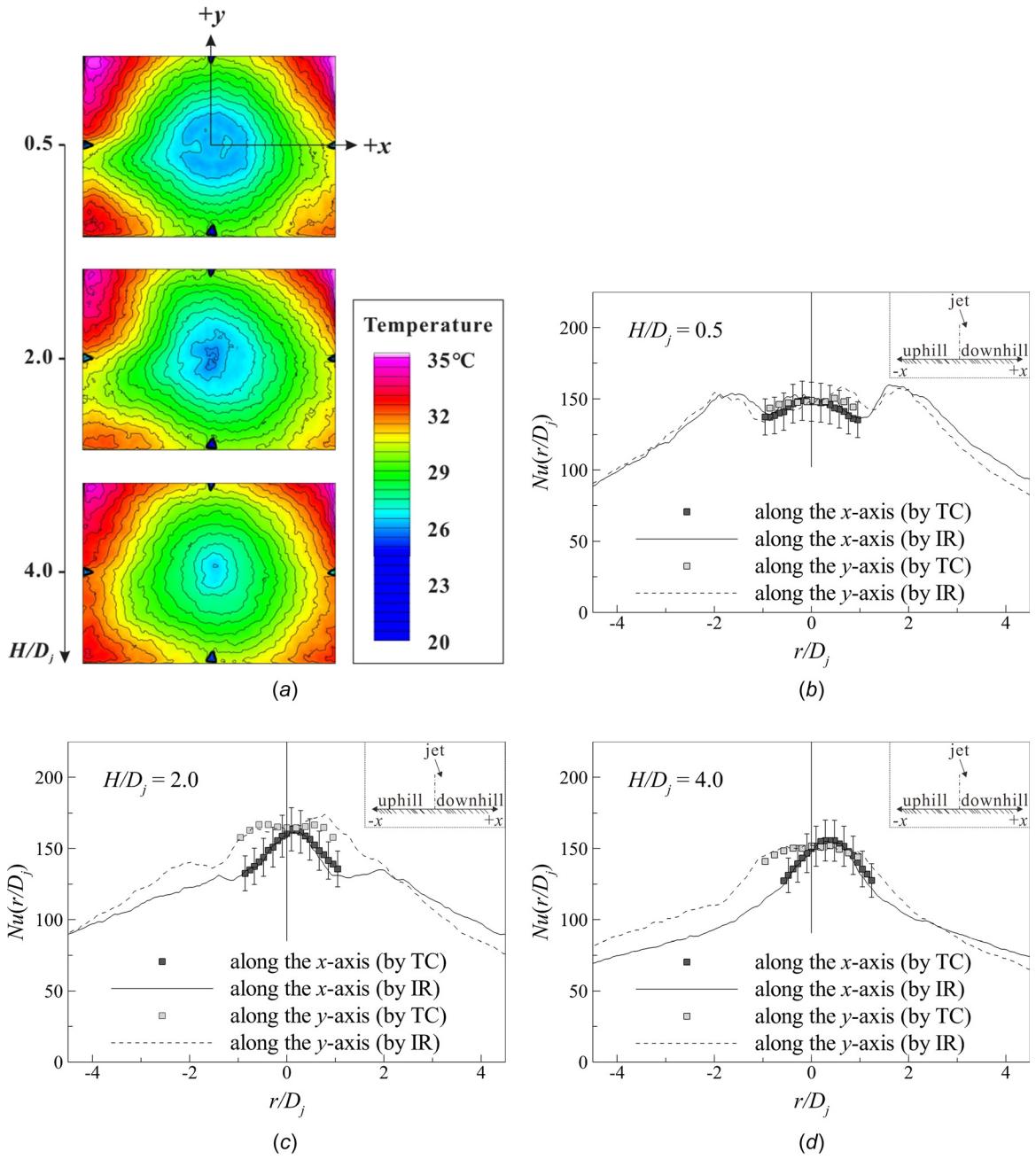

Fig. 5 Impingement of a single orifice jet at $Re_j = 20{,}000$: (*a*) temperature maps, (*b*) for $H/D_j = 0.5$, (*c*) for $H/D_j = 2.0$, and (*d*) for $H/D_j = 4.0$

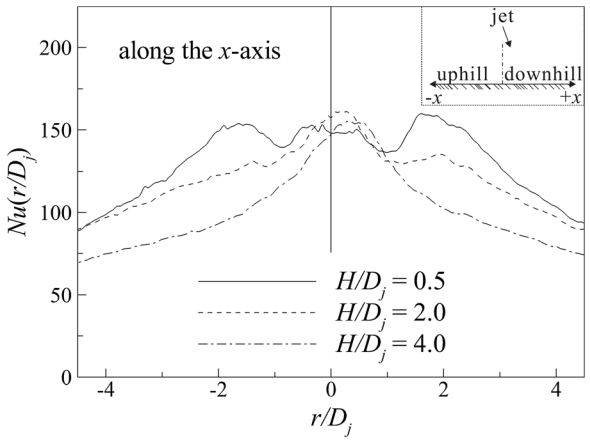

Fig. 6 Radial heat transfer distribution on flat target plate with varying H/D_j in x–z plane along x-axis

the film thermocouple (denoted by TC) were also included to validate the data obtained using the IR camera (denoted by IR). Only the short range of jet exit-to-target spacing, i.e., $H/D_j \leq 4.0$, was considered in this study since it was more engineering relevant, specific to internal cooling at the leading edge of a gas turbine blade [16].

With reference to Fig. 5(*b*), heat transfer distributions in both planes were very similar and largely symmetric with respect to the z-axis at $H/D_j = 0.5$. The Nusselt number decreased with increasing radial distance from the stagnation point, reaching local minima at $r/D_j = \pm 1.0$. Afterward, the Nusselt number turned to increase, reaching local peaks roughly at $r/D_j = \pm 2.0$, and then decrease again. The magnitude of the second heat transfer peaks was about 10% larger than the primary one at stagnation. Such high local heat transfer might be caused by local fluid acceleration in the gap between the jet exit and the target flat plate. It might also be attributed to a significant increase in local turbulence level [20–24]. Despite the skewed impingement of the orifice jet, the presence of symmetry in local heat transfer distributions on the target flat plate resulted from insufficient space for the jet to apparently skew. Consequently, no obvious asymmetry could be observed in the Nusselt number distributions.

At $H/D_j = 2.0$ (Fig. 5(*c*)), there exists an asymmetry in the heat transfer distribution. In the x–z plane (i.e., along the span of cylindrical chamber), a second peak was formed at $r/D_j = +2.0$ (on the downhill-side), while the other second peak formed at $r/D_j = -1.5$ (on the uphill-side). In the y–z plane, one pair of symmetric peaks was formed at $r/D_j = \pm 0.5$, instead of a single primary peak near the geometric stagnation point. On each side, additional second peaks formed at $r/D_j = \pm 2.0$. The most distinct difference from the foregoing case was the dissimilar distributions of local heat transfer between the two selected planes. In the x–z plane (i.e., along the span of cylindrical chamber), the primary peak was slightly shifted toward the positive x-axis. That is, the peak was located on the "downhill-side." This contrasted the typical feature associated with an inclined jet impinging on a target flat plate, often termed as "uphill-side shifting" [25,26].

At $H/D_j = 4.0$ (Fig. 5(*d*)), in the x–z plane, the primary peak still existed on the downhill-side, while the second peaks appeared to be diminished. In the y–z plane, the two peaks that formed near stagnation for $H/D_j = 0.5$ and 2.0 merged to form a single peak for $H/D_j = 4.0$, symmetric distributed with respect to the z-axis.

To directly compare how local heat transfer distribution in the x–z plane varied with H/D_j, the data of Figs. 5(*b*)–5(*d*) were extracted and plotted in Fig. 6. As H/D_j increased, the radial position of local primary peak changed such that it was located roughly on the uphill-side, at $H/D_j = 0.5$. In contrast, it was progressively moved toward the downhill-side and appeared to end up on the downhill-side at $r/D_j \sim 0.3$ for $H/D_j = 2.0$ and $r/D_j \sim 0.5$ for $H/D_j = 4.0$. It seemed that this behavior was at odds with previous studies of inclined jets (e.g., Ref. [26]). A classical tube jet impinging on a target surface with its nominal axis inclined from the normal to target plate always leads to an "uphill shifting" of the primary thermal peak [26]. The uphill shift is due to the displacement of the jet stagnation point away from the point where the geometric center of the jet meets the target plate (or geometric stagnation point). In previous studies, however, the jet was axisymmetric which is not present in this study as per Fig. 4(*b*). Due to the crescent shape of the jet profile, the geometric stagnation point of the jet itself is shifted. This shift is in the "downhill" direction according to $S(\alpha) = H(\tan(\alpha))$. Considering this shift, it could be shown (but not included) that the primary peak, for each of the three selected cases (i.e., $H/D_j = 0.5$, 2.0, and 4.0), resided on the uphill-side of the flat plate with respect to the actual geometric stagnation point.

4 Results of Multiple Asymmetric Orifice Jets

Built upon the established single asymmetric orifice jet whose characteristics differed from a single symmetric orifice jet, a single row of multiple orifice jets was systematically investigated. The jets had the fixed center-to-center spacing of $T/D_j = 4.0$, and each jet was discharged at $\mathrm{Re}_j = 20{,}000$. Similar to the foregoing discussion, upon impingement on an isoflux flat surface, key features like free jet patterns, centerline velocity variations, and local heat transfer distributions were detailed. Relative to a single asymmetric orifice jet, particular focus was placed upon how these features were altered by the presence of neighboring jets. Additionally, how stagnation point heat transfer varied with jet-to-flat plate distance was discussed.

4.1 Free Jet Patterns. The free jet pattern of coolant stream through the holes of a concave blunt orifice in the x–z plane was visualized. All five jets were discharged but only the central orifice jet was visualized in the water-tunnel. Similar to a single orifice jet, coherent structure-like vortices were shed from the edges of the central orifice in Fig. 7(*a*). The core of the orifice jet was skewed toward the positive x-direction, off from the orifice axis (z) by an angle of α. To quantify the skewness angle α, the radial profile of the axial velocity component of multiple orifice jets was measured at $2.0D_j$ and $4.0D_j$ downstream of the orifice exit. The results in Fig. 7(*b*) showed that the skewness angle measured from the z-axis was $\alpha \sim 15$ deg. In comparison, the reference single asymmetric orifice jet exhibited a much smaller skewness angle of $\alpha \sim 5$ deg. The higher skewness of multiple asymmetric jets may be attributed to the u-velocity component from neighboring orifice jets, which causes a transfer of momentum to an adjacent jet. Apart from the differing extents of skewness, however, the velocity fields for both single and multiple orifice jets do share common aspects. For example, both types of jet showed a symmetric velocity profile in their respective y–z planes, although the x–z planes showed asymmetric profiles which were skewed toward the positive x-direction.

To demonstrate how the shear layers developed by neighboring orifice jets interacted with each other, the shear layers on each side of two adjacent orifice jets were visualized in Fig. 7(*c*). The visualized image showed no apparent interaction between the coherent structures of the two jets, for all $H/D_j < 5.0$. Therefore, interaction of jet flows prior to impingement would not be expected when testing impingement heat transfer at $H/D_j = 0.5$, 2.0, and 4.0.

4.2 Centerline Velocity Variation. Similar to a single asymmetric orifice jet, the length of potential core (L_p) was estimated using the definition summarized by Gauntner et al. [19]. Accordingly, the central jet had a potential core length of $L_p = 0.6D_j$ along the z-axis, substantially shorter than $L_p = 1.7D_j$ for single asymmetric orifice jet (Fig. 8(*a*)). The orifice jets were skewed

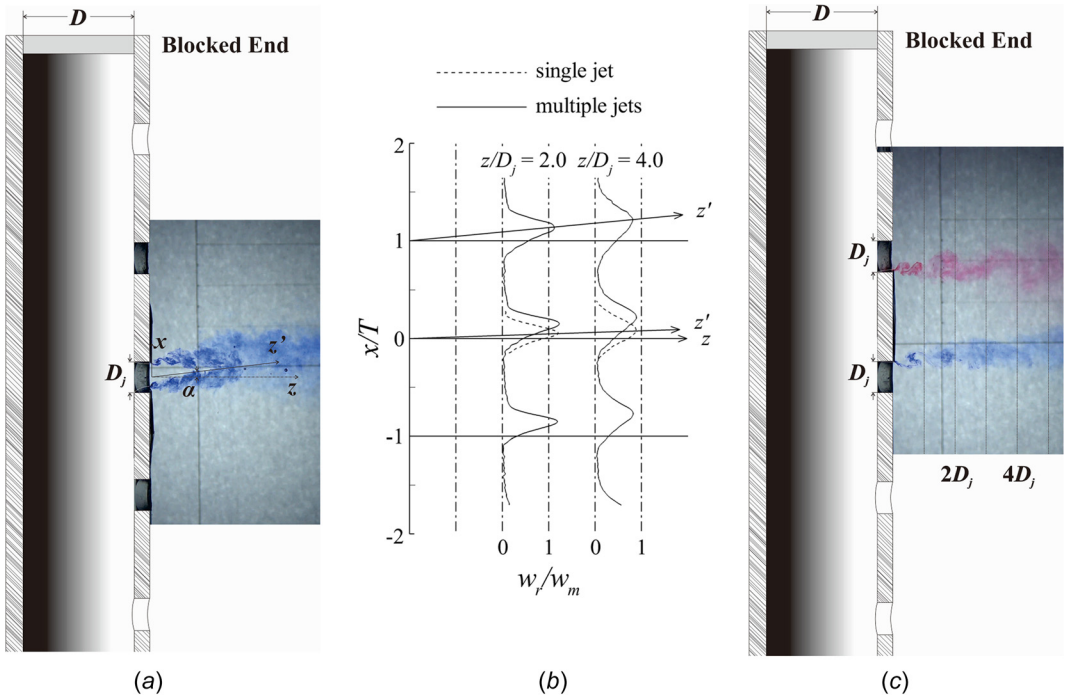

Fig. 7 Asymmetric orifice jet ($t/D_j = 0.5$) in free exit: (*a*) visualized jet patterns, (*b*) velocity profiles of asymmetric orifice jets in the *x*–*z* plane, and (*c*) visualized jet patterns

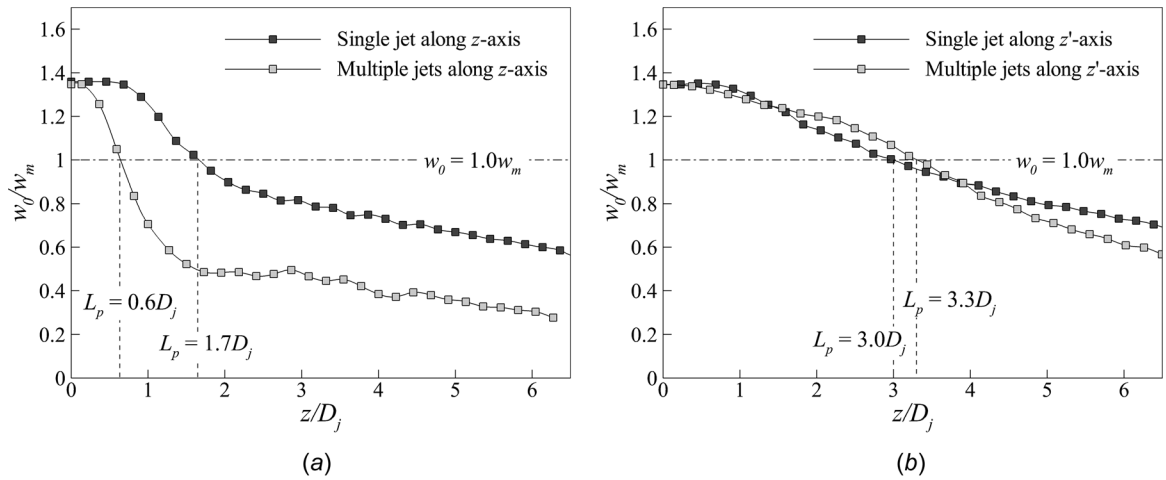

Fig. 8 Variation of centerline velocity for both single and multiple orifice jets along (*a*) *z*-axis and (*b*) *z*′-axis

with respect to the jet's nominal (z) axis, by $\alpha \sim 15$ deg for multiple asymmetric jets and by $\alpha \sim 5$ deg for single asymmetric jet. In consideration of this, for each jet type, the axial velocity components were remeasured along the skewed (z') axes. The results plotted in Fig. 8(*b*) demonstrated that the length of potential core (L_p) was roughly $L_p \sim 3.0D_j$ for both single and multiple orifice jets. This observation suggested that the presence of neighboring jets altered only the skewness, as other jet-flow characteristics remained approximately unchanged for the range of jet-to-jet spacing considered.

4.3 Stagnation Heat Transfer and Validation. Maximum heat transfer typically occurs near stagnation, except when the target surface is closely placed relative to jet exit(s), e.g., $H/D_j \leq 0.5$. Thus, the variation of stagnation point heat transfer with orifice exit-to-target plate spacing was of importance. In Fig. 9, the Nusselt number at stagnation (Nu_0) for a classical nozzle jet was compared to both symmetric and asymmetric orifice jets that impinged upon a flat target surface at similar jet Reynolds numbers ($\sim Re_j = 20{,}000$). A reference case was first established using symmetric jets with $t/D_j = 0.5$ and $t/D_j = 20.0$. Using the same impingement test rig with asymmetric jets for these two reference jets, the Nusselt number at stagnation point varying with flat plate spacing is shown in Fig. 9(*a*), and they are also separately compared with symmetric orifice jet with $t/D_j = 0.2$ [3] and classical nozzle jet with $t/D_j = 78.0$ [27]. The magnitude of Nusselt number and the location of maximum stagnation heat transfer show good agreement which provided the credibility of the present setups. The difference in the location of the maximum heat transfer at the stagnation point of the two orifice jets was attributed to the differences in relative thickness (t/D_j) between the current setup and that by Lee and Lee [3].

For the present asymmetric blunt orifice jets (Fig. 9(*b*)), heat transfer at stagnation (Nu_0) varied with relatively short H/D_j values, as follows. With increasing H/D_j, Nu_0 increased, peaking at

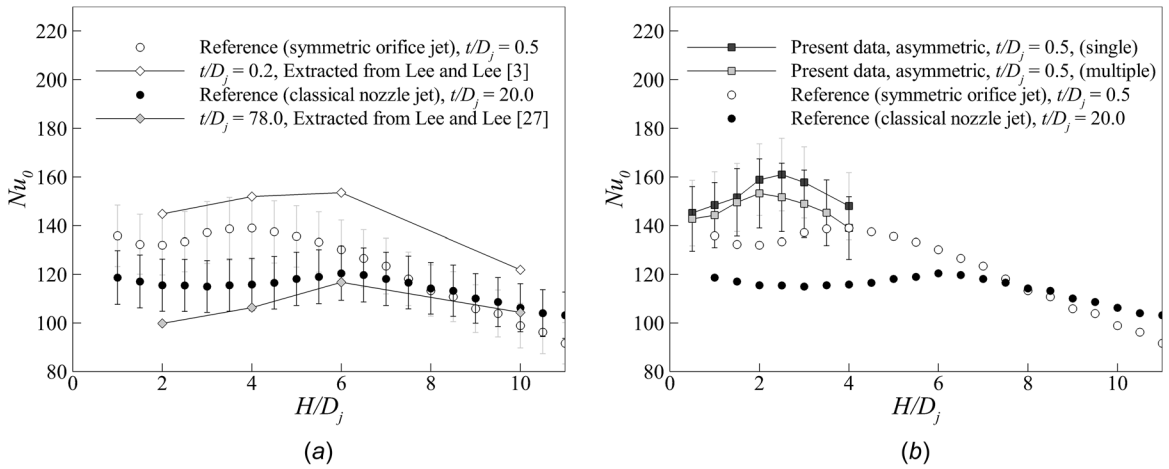

Fig. 9 Nusselt number at stagnation point (Nu_0) varying with flat plate target spacing at $Re_j = 20{,}000$: (*a*) experimental validation by symmetric single orifice jet and classical nozzle jet and (*b*) comparison of asymmetric single/multiple orifice jets with symmetric single orifice and classical nozzle jet

$H/D_j \sim 2.5$ for the single asymmetric orifice jet, followed by a monotonic decrease. In comparison, the single symmetric orifice jet ($t/D_j = 0.5$) achieved the peak Nu_0 at $H/D_j \sim 4.0$. The shortening of the peak location from $H/D_j \sim 4.0$ to 2.5 was substantial, but this was expected from the shortened potential core lengths observed for asymmetric jets. There is a direct correlation between the length of the potential core length and the H/D_j position at which the peak stagnation heat transfer occurs [28]. Indeed, for the same relative thickness $t/D_j = 0.5$, the potential core length measured for a single asymmetric orifice jet was substantially smaller than that measured for a single symmetric orifice jet: $L_p/D_j = 1.7$ along the z-axis (or $L_p/D_j \sim 3.0$ along the z'-axis) for the former and $L_p/D_j = 5.0$ for the latter (Fig. 4(*a*)). With the impingement of multiple asymmetric orifice jets, the Nu_0 variation with H/D_j was similar to that of single asymmetric orifice jet, but the peak Nu_0 occurred slightly upstream at $H/D_j \sim 2.0$.

Consider next the magnitude of stagnation point heat transfer shown in Fig. 9(*b*). All of the orifice jets were seen to exhibit superior heat transfer performance to the classical tube jet, i.e., $t/D_j = 20$. Among the single orifice jets considered, the asymmetric jet gave rise to a slightly higher Nu_0 when the target spacing was small (e.g., $H/D_j < 3$). With multiple asymmetric orifice jets, a slightly lower stagnation heat transfer was observed. This decrease in stagnation heat transfer is consistent with the observation of Koopman and Sparrow [14] for multiple nozzle jets. The decrease in stagnation heat transfer for multiple orifice jets is also possibly due to increased skewness of the multiple orifice jets ($\alpha \sim 15$ deg) compared to the single orifice jet ($\alpha \sim 5$ deg). An increase in inclination is known to result in a lower stagnation heat transfer [26].

It was worth noting that the fluidic mechanism responsible for the observed longitudinal locations of the peak Nu_0 was the apparent variation of turbulent strength along the jet axis. Specifically, for each fully developed turbulent jet, the peak Nu_0 value typically occurred at a slight downstream distance from the tip of potential core, where the turbulent strength is known to be at maximum [20,28]. This argument appeared to be valid for the reference-cases (i.e., symmetric orifice jets), where the peak Nu_0 was located at $H/D_j = 6.0$, with $L_p/D_j = 5.0$. However, despite the potential core length of approximately $L_p/D_j \sim 3.0$, there appears to be a mismatch between the actual and expected locations of the peak Nu_0. Specifically, for single asymmetric orifice jet, the observed peak was located at $H/D_j = 2.5$, while for multiple asymmetric orifice jets the peaks were at $H/D_j = 2.0$. As the peak Nu_0 was clearly positioned inside the potential core, two possibilities were surmised here: (1) the turbulent strength argument may be invalid in this case, or (2) the peak turbulence strength along the jets' axes did not occur downstream of their respective potential cores. For clarification, we believe that detailed turbulence properties of both single and multiple asymmetric orifice jets, having unique potential core shapes as shown in Fig. 4(*b*), were required, which were nonetheless out of the scope of this study.

4.4 Local Heat Transfer Distribution on a Target Flat Plate. Consider next local heat transfer patterns on a flat plate impinged by multiple asymmetric orifice jets, with center-to-center spacing fixed at $T/D_j = 4.0$. Data for single asymmetric orifice jet were also included as reference to highlight any dissimilar features. For both cases, the jet Reynolds numbers were fixed at $Re_j = 20{,}000$. It should be noted that, for multiple asymmetric orifice jets, the jet Reynolds number in each orifice hole might have differed, since there were no special contrivances made to ensure an equal flowrate through every hole. This was maintained in this study as such contrivances were not expected in engineering applications. The proceeding discussion was thus focused upon the centermost orifice hole, for selected short jet-to-target plate spacing (i.e., $H/D_j = 0.5$, 2.0, and 4.0) set along the nominal orifice jet axis (i.e., the z-axis).

4.4.1 At $H/D_j = 0.5$. Figure 10 presented local temperature contours on a flat plate, as well as calculated Nusselt numbers along the x-axis at $H/D_j = 0.5$. Similar to a single asymmetric orifice jet, the overall temperature map of Fig. 10(*a*) exhibited a crescent shape core region for each jet, within which a higher local heat transfer region was evident.

To compare the thermal performance of single and multiple asymmetric orifice jets, Nusselt number distributions near stagnation were obtained using both infrared thermography (denoted as "by IR") and thermocouple (denoted as "by TC"), as shown in Fig. 10(*b*). The thermocouple and infrared readings showed good agreement. Further, the measurements indicated that both types of jet thermally behaved in a similar manner, with the multiple asymmetric orifice jets having a slightly lower stagnation point heat transfer at the jet Reynolds number of 20,000 as was also noted in Fig. 9(*b*).

Along the span of a feed passage, i.e., x-axis, the Nusselt number distributions of Fig. 10(*b*) showed peaks in heat transfer that were roughly coinciding with geometric stagnation points (i.e., $x/T = -1.0$, 0.0, and 1.0), even though the jets were initially skewed by $\alpha \sim 15$ deg. Such a coincidence was due to the proximity of the flat plate to orifice exits, which resulted in the jet's inherent skewness going undetected.

Local heat transfer decreased with increasing distance from the primary peak at stagnation, after which second peaks formed

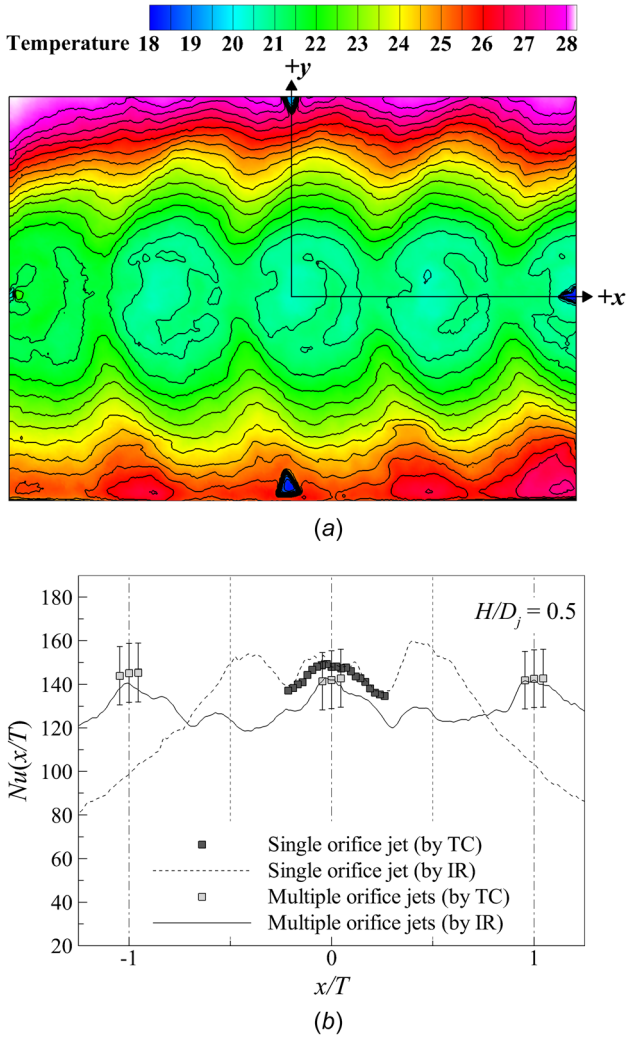

Fig. 10 Local heat transfer on flat plate at $H/D_j = 0.5$: (*a*) temperature contours and (*b*) Nusselt number distribution

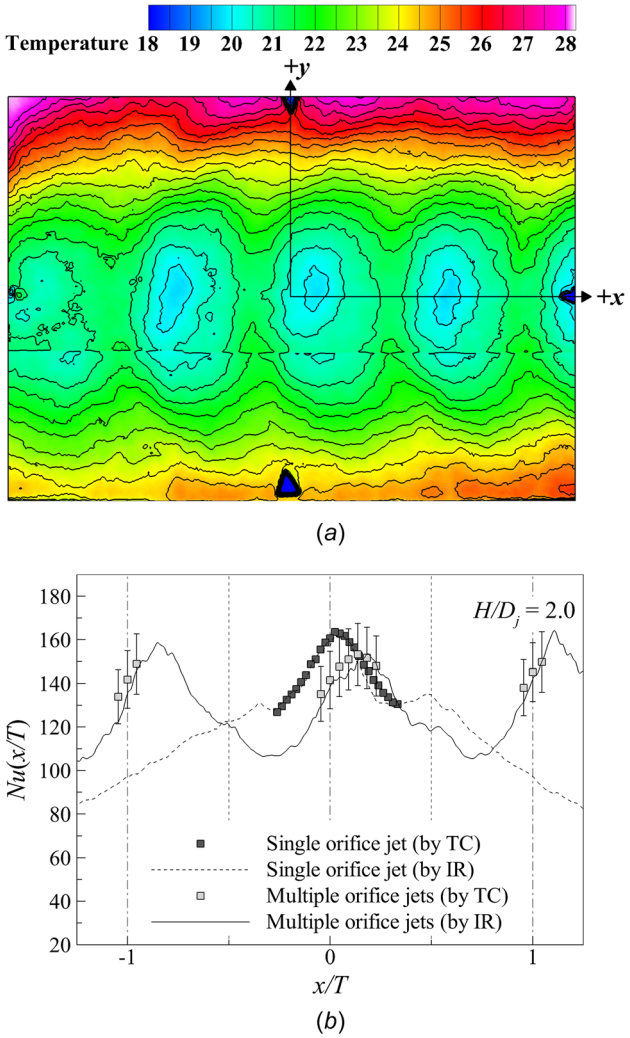

Fig. 11 Local heat transfer on flat plate at $H/D_j = 2.0$: (*a*) temperature contours and (*b*) Nusselt number distribution

roughly at midinterjet spacing ($x/T = \pm 0.5$). For multiple asymmetric orifice jets, the second peaks were only 13% lower in magnitude when compared with the corresponding primary peaks. These second peaks could be due to the collision between neighboring wall jet flows [14,29]. For the single asymmetric orifice jet, at $H/D_j = 0.5$ (i.e., no presence of neighboring jets), the more distinct second peaks were likely caused by a different fluidic mechanism—transition of laminar boundary layer to turbulent boundary layer.

In summary, with $T/D_j = 4.0$ and $H/D_j = 0.5$, the multiple asymmetric orifice jets could provide a more uniform heat removal from a target flat plate. There is also a similar level of stagnation point heat transfer, albeit at the added expense of increased coolant flow compared to that of a single asymmetric orifice jet at the same Reynolds number.

4.4.2 At $H/D_j = 2.0$. Upon increasing H/D_j from 0.5 to 2.0, the crescent shape core region became considerably less distinct but was still visible in Fig. 11(*a*). Calculated Nusselt numbers based on the extracted data from Fig. 11(*a*) were displayed in Fig. 11(*b*). These results indicated that the second thermal peaks were substantially reduced in magnitude compared to those in the case of $H/D_j = 0.5$. At this spacing ($H/D_j = 2.0$), wall-jets in the multiple asymmetric orifice jets were substantially diffused before collision, leading to weakened fountain jets. For a single asymmetric orifice jet, the secondary peaks induced by boundary layer transition were also weakened due to reduced local acceleration in the vicinity of stagnation. This was because the static pressure at stagnation decreased as a result of the relatively lower arrival velocity at $H/D_j = 2.0$ (Fig. 4).

The geometric stagnation points shifted away from the center axis ($x/T = 0$), toward the downhill-side (along the x-axis), for both single and multiple asymmetric orifice jets. This resulted in the shift in the peaks to the downhill-side. The extent of shifting was more pronounced for the latter case, as shown in Fig. 11(*b*), due to relatively higher skewness angle ($\alpha \sim 15$ deg). By correcting the Nusselt number distributions to account for jet skewness, the expected uphill-side shifts of primary peaks (for both multiple and single asymmetric orifice jets) could be observed (but not included). The extent of uphill-side shifting was greater for multiple asymmetric orifice jets compared to a single asymmetric orifice jet, as the former had a characteristically larger skewness angle (~15 deg) than the latter (~5 deg).

4.4.3 At $H/D_j = 4.0$. At $H/D_j = 4.0$, there was a clear disappearance of secondary thermal peaks for a single asymmetric orifice jet. For multiple asymmetric orifice jets, however, there existed very weak second peaks, as shown in Figs. 12(*a*) and 12(*b*). The former suggested that, at this H/D_j value, transition from laminar boundary layer to turbulent boundary layer was likely absent. This should be expected, since the target surface was positioned outside the potential core. On the other hand, the latter indicated that the wall-jets had lost a great amount of momentum, due to diffusion and dissipation within the mixing

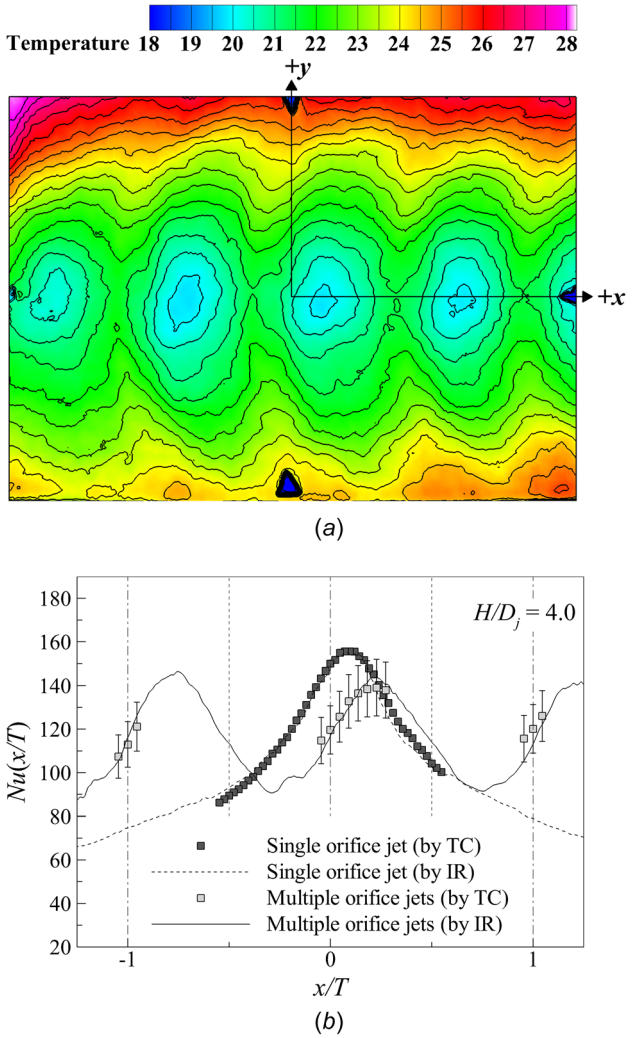

Fig. 12 Local heat transfer on flat plate at $H/D_j = 4.0$: (*a*) temperature contours and (*b*) Nusselt number distribution

layers. Consequently, the collision of wall-jets with those from neighboring impinging jets was thus relatively weak, resulting in correspondingly weak second thermal peaks.

Similar to the previous two H/D_j cases, the primary peaks were resident on the downhill-side with respect to the z-axis due to the relatively higher skewness angle ($\alpha \sim 15$ deg) of the multiple orifice jets. After correcting local Nusselt numbers distributed on the flat plate according to corresponding skewness values, uphill-side shifting of the primary peak became visible for both single and multiple orifice jets. A more severe shift was also evident in the case of multiple asymmetric orifice jets based on the higher skewness for the multiple orifice jets and increase in the shift of jet geometric center with increased skewness according to $S(\alpha) = H(\tan(\alpha))$.

4.5 Local Heat Transfer Distribution in the *y–z* Plane on a Target Flat Plate. In the y–z plane, the jet streams were configurationally discharged through a concave orifice and were expected to bifurcate symmetrically with respect to the x-axis. Two selected H/D_j cases, i.e., $H/D_j = 0.5$ and 4.0, were considered separately in comparison with a single asymmetric orifice jet.

Data sets were extracted from Figs. 10(*a*) and 12(*a*) along the y-axis. Since detailed thermofluidic characteristics in the y–z plane deserve a separate and in-depth analysis which is out of the scope of this study, only an overall comparison of local heat transfer distributions along the y-axes was made below, starting from the nominal stagnation points, i.e., $x = 0$ and $z = H$.

At $H/D_j = 0.5$, for both single and multiple orifice jets, local heat transfer distributions were approximately symmetric about the x-axis, as evidenced from the results displayed in Fig. 13(*a*). There is nonetheless a subtle asymmetry, due to imperfect positioning and fabrication of each orifice. Radially along the y-axis, there existed a second thermal peak in addition to the primary peak near stagnation. The secondary peaks were thought to be associated with jet acceleration through a gap between the orifice exit and the flat plate. The magnitude of the secondary peak in the single orifice jet case was substantially higher compared with the multiple orifice jets, due likely to jet-to-jet interference but further investigation is needed to quantify its effect. The radial (or lateral) locations of the second peaks formed by the multiple jets were located at $r/D_j \sim 1.5$. This indicated that the cause of secondary peaks might have been a transition from laminar to turbulent boundary layer, rather than flow acceleration mentioned above given that both cases have the same H/D_j gap. In the y–z plane, the wall-jets departing from stagnation experienced an adverse pressure gradient due to a diverging flow area. Thus, it might be possible for transition to take place in the case of multiple asymmetric orifice jets. At present, however, it remained elusive why such a transition was not evident in the case of single asymmetric orifice jet, which again required further clarification.

At $H/D_j = 4.0$, for both single and multiple asymmetric orifice jet, the flat plate was positioned outside the potential core: as a result, secondary thermal peaks could not be observed in either case. The multiple asymmetric orifice jets exhibited a relatively

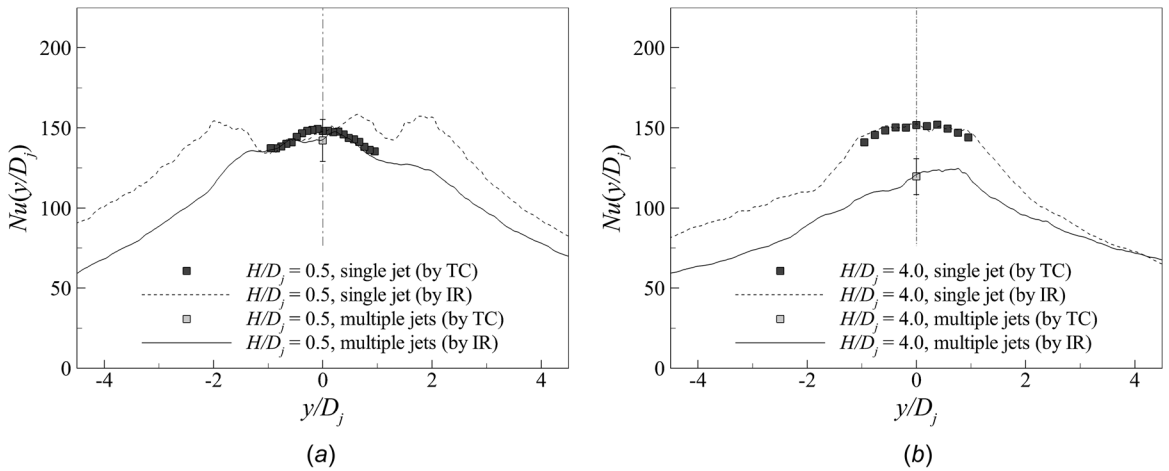

Fig. 13 Local heat transfer distribution on flat plate in *y–z* plane at $x = 0$ for (*a*) $H/D_j = 0.5$ and (*b*) $H/D_j = 4.0$

lower cooling performance, as shown in Fig. 13(*b*). This is likely due to the jets being skewed by different amounts along the *x*-axis, the line $x/T = 0$ does not necessarily pass through any of the stagnation points. Relatively speaking, the line $x = 0$ in the single jet case is closer to the geometric stagnation point. Consequently, along $x = 0$, the multiple asymmetric jets appeared to achieve a far lower thermal performance than the single asymmetric orifice jet.

In summary, thermal distribution in the *y*–*z* plane consistently followed conventional pattern, such as: (a) symmetric distribution with respect to jet axis, (b) appearance of secondary thermal peaks associated with either flow acceleration in the very proximity of the jet to target plate or transition of laminar to turbulent boundary layer, and (c) disappearance of secondary thermal peaks when positioned outside potential core. However, additional study is required due to unique geometric and fluidic aspects that are likely to be found in the *y*–*z* plane, such as divergent flow area and jet-to-jet interference among skewed asymmetric orifice jets.

5 Conclusions

This study presented impingement cooling of a flat plate emitting constant heat flux, by inline multiple nonaxisymmetric orifice jets, with a fixed relative thickness of $t/D_j = 0.5$, jet-to-jet spacing of $T/D_j = 4.0$, and fixed jet Reynolds number of 20,000. A series of experiments were conducted to systematically characterize the thermofluidic behavior, with the orifice exit-to-flat plate spacing (H/D_j) varied from 0.5 to 4.0. Newly found aspects of impingement cooling by asymmetric orifice jets were summarized as follows.

(a) Due to a skewed incidence of coolant stream upstream of the orifice holes and the curvature of each orifice, the resulting orifice jets were not only nonaxisymmetric but also skewed relative to the orifice axis, forming distinct crescent-moon-like potential cores.
(b) The off-axis skewness in the case of multiple asymmetric jets was substantially increased, approximately thrice that found in the case of single asymmetric jet.
(c) The skewed asymmetric jets mimicked inclined jets, yet with asymmetric entrainment, thus not only promoting faster mixing and longitudinal decay of momentum but also causing shorter potential cores than symmetric jets discharged from conventional nozzles and orifices.
(d) Secondary thermal peaks were formed in the *x*–*z* planes of asymmetric orifice jets. For multiple asymmetric orifice jets, secondary peaks formed at the midpoint of interjet spacing, due to collision of wall-jets. For a single asymmetric orifice jet, secondary peaks were also observed, due to transition to turbulence in the boundary layer of the wall-jet.
(e) Multiple asymmetric jets provided more uniform heat transfer distributions compared to single asymmetric orifice jet, albeit with slightly lower heat transfer at stagnation points.
(f) At small H/D_j values (e.g., $H/D_j \leq 4.0$), asymmetric orifice jets exhibited superior heat removal capacity compared to classical nozzle jets and slightly higher heat transfer near stagnation compared to symmetric orifice jets.

Funding Data

- National Natural Science Foundation of China (Grant Nos. 11972185 and 12032010; Funder ID: 10.13039/501100001809).
- Open Fund of the State Key Laboratory of Mechanics and Control of Mechanical Structures (Grant Nos. MCMS-I-0219K01 and MCMS-E-0219K02; Funder ID: 10.13039/501100011402).
- One-Belt-One-Road Innovative Talent Exchange Programme for Foreign Experts (Grant No. DL20200010006), China.

Nomenclature

D = cylindrical chamber diameter in water-tunnel, m
D_j = jet diameter, m
H = spacing between jet exit plane and target surface, m
h_s = local heat transfer coefficient on target surface, W/(m^2 K)
IR = data from infrared thermography
k_f = thermal conductivity of working fluid (air), W/(m K)
L_p = length of potential core, m
Nu_0 = Nusselt number at stagnation point of target surface
q''_{cond} = conduction loss, W/m^2
q''_{net} = net heat flux emitted by etched foil heater, W/m^2
$q''_{\mathrm{net,\,IR}}$ = net heat flux emitted by stainless-steel shim stock heater, W/m^2
q''_{rad} = radiation loss, W/m^2
q''_t = total input heat flux supplied to etched foil heater, W/m^2
$q''_{t,\,\mathrm{IR}}$ = total input heat flux supplied to stainless-steel shim stock heater, W/m^2
r = radial coordinate from jet centerline
R_{loss} = relative heat loss
Re_j = Reynolds number based on orifice diameter
t = orifice hole thickness, m
T = center-to-center spacing between two adjacent jets, m
T_a = ambient air temperature, K
T_b = back side temperature of bakelite plate, K
T_e = air temperature at jet exit, K
T_s = local target surface temperature, K
TC = data from thermocouples
w_e = centerline axial velocity component at jet exit, m/s
w_m = bulk-mean flow velocity component at jet exit, m/s
w_r = time-averaged axial velocity at a specific radial location, m/s
w_0 = centerline axial velocity component, m/s
x = an axis coinciding with the span of cylindrical chamber (or feed passage)
y = an axis perpendicular to both the cylinder chamber span and nominal jet axis
z = longitudinal axis coinciding with nominal jet axis
z' = actual jet axis that is skewed

Greek Symbols

α = skewed angle of jet
ϵ = emissivity of gray surface
μ = dynamic viscosity, N s/m^2
ρ = density, kg/m^3
σ = Stefan–Boltzmann constant, W/(m^2 K^4)

References

[1] Moon, S. W., and Lau, S. C., 2003, "Heat Transfer Between Blockages With Holes in a Rectangular Channel," ASME J. Heat Transfer-Trans. ASME, **125**(4), pp. 587–594.
[2] Shakouchi, T., and Kito, M., 2012, "Heat Transfer Enhancement of Impinging Jet by Notched-Orifice Nozzle," *An Overview of Heat Transfer Phenomena*, S. N. Kazi, ed., InTech, London, pp. 441–468.
[3] Lee, J., and Lee, S.-J., 2000, "The Effect of Nozzle Configuration on Stagnation Region Heat Transfer Enhancement of Axisymmetric Jet Impingement," Int. J. Heat Mass Transfer, **43**(18), pp. 3497–3509.
[4] Quinn, W. R., 2006, "Upstream Nozzle Shaping Effects on Near Field Flow in Round Turbulent Free Jets," Eur. J. Mech. - B/Fluids, **25**(3), pp. 279–301.
[5] El Hassan, M., and Meslem, A., 2010, "Time-Resolved Stereoscopic Particle Image Velocimetry Investigation of the Entrainment in the Near Field of Circular and Daisy-Shaped Orifice Jets," Phys. Fluids, **22**(3), p. 035107.
[6] Miller, D. R., and Comings, E. W., 1960, "Force-Momentum Fields in a Dual-Jet Flow," J. Fluid Mech., **7**(2), pp. 237–256.
[7] Knystautas, R., 1964, "The Turbulent Jet From a Series of Holes in Line," Aeronaut. Q., **15**(1), pp. 1–28.
[8] Nasr, A., and Lai, J. C. S., 1997, "Two Parallel Plane Jets: Mean Flow and Effects of Acoustic Excitation," Exp. Fluids, **22**(3), pp. 251–260.

[9] Ghahremanian, S., Svensson, K., Tummers, M. J., and Moshfegh, B., 2014, "Near-Field Development of a Row of Round Jets at Low Reynolds Numbers," Exp. Fluids, **55**, p. 1789.
[10] Okamoto, T., Yagita, M., Watanabe, A., and Kawamura, K., 1985, "Interaction of Twin Turbulent Circular Jet," Bull. JSME, **28**(238), pp. 617–622.
[11] Glaser, H., 1962, "Untersuchungen an Schlitz- und Mehrdusenanordnungen bei der Trocknung feuchter Oberflachen durch Warmluftstrahlen," Chem. Ing. Tech., **34**(3), pp. 200–207.
[12] Saripalli, K. R., 1983, "Visualization of Multijet Impingement Flow," AIAA J., **21**(4), pp. 483–484.
[13] Saripalli, K., 1985, "Laser Doppler Velocimeter Measurements in a 3-D Impinging Twin-Jet Fountain Flow," AIAA Paper No. 85-4036.
[14] Koopman, R. N., and Sparrow, E. M., 1976, "Local and Average Transfer Coefficients Due to an Impinging Row of Jets," Int. J. Heat Mass Transfer, **19**(6), pp. 673–683.
[15] Goldstein, R. J., and Timmers, J. F., 1982, "Visualization of Heat Transfer From Arrays of Impinging Jets," Int. J. Heat Mass Transfer, **25**(12), pp. 1857–1868.
[16] Krause, D. A., Soechting, F. O., Mongillo, D. J., Jr., and Zelesky, M. F., 1999, "Airfoil Cooling," European Patent No. EP-0-896-127-A2.
[17] Coleman, H. W., and Steele, W. G., 2009, *Experimentation, Validation, and Uncertainty Analysis for Engineers*, 3rd ed., Wiley, Hoboken, NJ.
[18] Abramovich, G. N., 1963, *The Theory of Turbulent Jets*, The MIT Press, Cambridge, MA.
[19] Gauntner, J. W., Livingood, J. N. B., and Hrycak, P., 1970, "Survey of Literature on Flow Characteristics of a Single Turbulent Jet Impinging on a Flat Plate," NASA, Washington, DC, Report No. NASA TN D-5652.
[20] Nguepnang, M. A., Boer, M., and Kim, T., 2016, "Stagnation Heat Transfer on a Concave Surface Cooled by Unconfined Slot Jet," J. Thermophys. Heat Transfer, **30**(3), pp. 558–566.
[21] Katti, V., and Prabhu, S. V., 2008, "Experimental Study and Theoretical Analysis of Local Heat Transfer Distribution Between Smooth Flat Surface and Impinging Air Jet From a Circular Straight Pipe Nozzle," Int. J. Heat Mass Transfer, **51**(17–18), pp. 4480–4495.
[22] Nirmalkumar, M., Katti, V., and Prabhu, S. V., 2011, "Local Heat Transfer Distribution on a Smooth Flat Plate Impinged by a Slot Jet," Int. J. Heat Mass Transfer, **54**(1–3), pp. 727–738.
[23] Gulati, P., Katti, V., and Prabhu, S. V., 2009, "Influence of the Shape of the Nozzle on Local Heat Transfer Distribution Between Smooth Flat Surface and Impinging Air Jet," Int. J. Therm. Sci., **48**(3), pp. 602–617.
[24] Lytle, D., and Webb, B. W., 1994, "Air Jet Impingement Heat Transfer at Low Nozzle-Plate Spacings," Int. J. Heat Mass Transfer, **37**(12), pp. 1687–1697.
[25] Martin, H., 1977, "Heat and Mass Transfer Between Impinging Gas Jets and Solid Surfaces," *Advances in Heat Transfer*, J. P. Hartnett and T. F. Irvine, eds., Elsevier, Amsterdam, The Netherlands, pp. 1–60.
[26] Wang, X. L., Yan, H. B., Lu, T. J., Song, S. J., and Kim, T., 2014, "Heat Transfer Characteristics of an Inclined Impinging Jet on a Curved Surface in Crossflow," ASME J. Heat Transfer-Trans. ASME, **136**(8), p. 081702.
[27] Lee, J., and Lee, S.-J., 1999, "Stagnation Region Heat Transfer of a Turbulent Axisymmetric Jet Impingement," Exp. Heat Transfer, **12**(2), pp. 137–156.
[28] Gardon, R., and Akfirat, J. C., 1965, "The Role of Turbulence in Determining the Heat-Transfer Characteristics of Impinging Jets," Int. J. Heat Mass Transfer, **8**(10), pp. 1261–1272.
[29] Barata, J. M., 1996, "Fountain Flows Produced by Multiple Impinging Jets in a Crossflow," AIAA J., **34**(12), pp. 2523–2530.